RESEARCH ARTICLE | SEPTEMBER 26 2025

Mapping causal patterns in crystalline solids

Kamyar Barakati ; Christopher T. Nelson; Anna N. Morozovska ; Maxim A. Ziatdinov ; Eugene A. Eliseev ; Xiaohang Zhang ; Ichiro Takeuchi ; Sergei V. Kalinin

APL Mach. Learn. 3, 036117 (2025)
https://doi.org/10.1063/5.0284465

Mapping causal patterns in crystalline solids

Cite as: APL Mach. Learn. 3, 036117 (2025); doi: 10.1063/5.0284465
Submitted: 8 June 2025 • Accepted: 4 September 2025 •
Published Online: 26 September 2025

Kamyar Barakati,[1,a)] Christopher T. Nelson,[2] Anna N. Morozovska,[3] Maxim A. Ziatdinov,[4] Eugene A. Eliseev,[5] Xiaohang Zhang,[6] Ichiro Takeuchi,[6] and Sergei V. Kalinin[1,4,b)]

AFFILIATIONS

[1] Department of Materials Science and Engineering, University of Tennessee, Knoxville, Tennessee 37996, USA
[2] Center for Nanophase Materials Sciences, Oak Ridge National Laboratory, Oak Ridge, Tennessee 37831, USA
[3] Institute of Physics, National Academy of Sciences of Ukraine, 46, pr. Nauky, 03028 Kyiv, Ukraine
[4] Pacific Northwest National Laboratory, Richland, Washington 99354, USA
[5] Frantsevich Institute for Problems in Materials Science, National Academy of Sciences of Ukraine, 3, str. Omeliana Pritsaka, 03142 Kyiv, Ukraine
[6] Department of Materials Science and Engineering, University of Maryland, College Park, Maryland 20742, USA

[a)] **Author to whom correspondence should be addressed:** kbarakat@vols.utk.edu
[b)] sergei2@utk.edu

ABSTRACT

The evolution of the atomic structures of the combinatorial library of Sm-substituted thin film $BiFeO_3$ along the phase transition boundary from the ferroelectric rhombohedral phase to the non-ferroelectric orthorhombic phase is explored using scanning transmission electron microscopy. Localized properties, including polarization, lattice parameter, and chemical composition, are parameterized from atomic-scale imaging, and their causal relationships are reconstructed using a linear non-Gaussian acyclic model. This approach is further extended to explore the spatial variability of the causal coupling using the sliding window transform method, which revealed that new causal relationships emerged at both the expected locations, such as domain walls and interfaces, and at additional regions forming clusters in the vicinity of the walls or spatially distributed features. While the exact physical origins of these relationships are unclear, they likely represent nanophase-separated regions in the morphotropic phase boundaries. Overall, we posit that an in-depth understanding of complex disordered materials away from thermodynamic equilibrium necessitates understanding not only the generative processes that can lead to observed microscopic states but also the causal links between multiple interacting subsystems.

Foundational advances in condensed matter physics and materials science are inseparably linked with developments in characterization methods that provide progressively more detailed information on the structure and functionality of matter. The introduction of X-ray scattering methods by Bragg over a century ago enabled the first determinations of the atomic structure of solids and stimulated the emergence of a physical formalism based on reciprocal space descriptions, including zone theory, quasiparticles, and order parameter-based theories. In this case, observables such as structure factors or inelastic scattering can be directly matched to the theoretical descriptors. Comparatively, details on how these structures emerge were of lesser interest, with the connections established via average defect concentrations and the potential presence and dynamics of extended defects.

Not surprisingly, this approach was limited for materials that lacked long-range translational symmetry, including structural, dipole, and spin glasses.[1,2] For these systems, kinetic limitations during the formation process led to the formation of high defect densities and frustrated bond networks. Interestingly, systems lacking long-range order also emerge as a result of geometric frustration and symmetry mismatch between interacting subsystems and, in principle, correspond to (one of the) highly degenerate potential energy minima separated by high activation barriers. These materials have rapidly become one of the central topics of condensed matter physics

due to both fundamental physical interest and the unique functional properties they exhibit.[3–5] However, studying these materials via scattering methods has proven to be highly non-trivial and remains an active area of research.[6–8]

The emergence of atomically resolved scanning probe microscopy (SPM) over the last two decades of the twentieth century[9–11] and especially the rapid progress in aberration-corrected (scanning) transmission electron microscopy (STEM)[12–14] and atom probe tomography (APT) during the last decade have made the observation of the atomic structures and compositions of 2D and small-volume "bulk" materials routine. Consequently, material structures and chemistries are becoming accessible for examination at the individual atom level (APT, tomographic reconstructions in STEM). In other cases, information on the atomic column positions and compositions averaged across the sample thickness is available. However, advances in visualizing the atomic structures necessitate equivalent progress in the development of a corresponding descriptive language that allows both parsimonious descriptions of observed structures (i.e., local equivalent of a primitive cell) and can be used to build physical models.

In many cases, descriptions of atomic-level structures have been accomplished using macroscopic descriptors such as Fourier transforms, with the amplitude interpreted similarly to scattering studies and phases used as additional information, such as for geometric phase analysis in (S)TEM.[15–24] In several cases, this approach was adapted to the sliding window transform[25–28] to explore variability within an imaged region. Alternatively, identification of atomic-level features allows for strategies based on graph theory, molecular fragments, or other descriptors.[29,30] The atomic and continuous descriptors can be further combined as demonstrated in Ref. 31. Here, the use of dimensionality reduction methods that allow for the incorporation of invariance enables parsimonious descriptions. However, these models invariably build a correlative model of the solid structure, in which the number of required descriptors can still be exceedingly large. For example, describing point defects in solids or potential atomic configurations in solid solutions far from a phase transition is relatively straightforward, whereas extended defects or materials in the vicinity of a phase transition require a significantly larger and potentially divergent number of descriptors.

The alternative approach for descriptions of solids can be based on generative models. For example, the description of a (potentially structurally complex) microstructure belonging to the Ising universality class requires only the knowledge of the corresponding exchange integrals. This approach directly underpins multiple areas of theoretical condensed matter and statistical physics, where the lattice models or force fields form the basis for the description.[32] Interestingly, while the prediction of the structure and functionality from theoretical models is by now extremely well developed, the inverse problem of reconstruction of the model parameters from experimental observations is only at the beginning, with only a few recent examples of generative model reconstructions.[33,34]

However, the discovery of a generative model is not always sufficient to fully understand the material's physics. For example, in morphotropic ferroelectrics, the dopants can pin polarization; however, polarization instabilities can, in turn, drive cation redistribution. Similarly, can we establish whether the average electron concentration or local chemistry drives distortion patterns in doped chalcogenides? Such questions can be answered by performing a macroscopic experiment. For example, the electron concentration effect and chemical environment can be separated by electrostatic gating in field-effect devices. Similarly, ferroelectric instability can be tuned by pressure independent of composition. However, in many cases, direct experiments are expensive or impossible or are associated with additional confounding effects. For example, electrostatic gating to change the electron concentration often couples to chemical changes in a material. Hence, the question is whether the local observations of multiple spatially resolved degrees of freedom in STEM can be used to analyze the causal mechanisms that are operational in real materials.

Here, we explore causal interactions in cation-substituted multiferroic materials across the ferroelectric–non-ferroelectric phase transition boundary from atomically resolved STEM measurements on the combinatorial library of Sm-doped $BiFeO_3$. A linear non-Gaussian acyclic model (LiNGAM)[35] is used to reconstruct the causal chain and estimate the linear connections between the observed variables. This approach is further adapted to explore the spatial variability and concentration dependence of these interactions.

To illustrate the concepts involved in causal analysis, Fig. 1 shows the simplified cause-and-effect chain between three variables, z_0, z_1, and z_2. As an example, z_0 can be the partial pressure of a gas, z_1 is the concentration of oxygen vacancies, and z_2 is the conductivity of the material; however, similar examples can be chosen from any physical subfield. We assume that the relationship between these parameters is given by

$$z_1 = 3z_0 + \epsilon_1, \tag{1a}$$

$$z_2 = -6z_1 + \epsilon_2, \tag{1b}$$

where ϵ_1 and ϵ_2 are random noise with a uniform distribution on $(-1, 1)$. We further assume that a set of observables (z_0, z_1, z_2) are available for observation. When the causal physics of the process are known, the analysis of the data is straightforward. Regression of z_1 on z_0, $z_1 = z_1(z_0)$, yields the dependence of the vacancy concentration on gas pressure, whereas regression $z_2(z_1)$ yields the dependence of conductivity on vacancy concentration, and $z_2(z_0)$ yields the dependence of conductivity on gas pressure. Note that implicit in this analysis is that there are no other active mechanisms; for example, the temperature (which can affect both conductivity and vacancy concentration) is constant, there is no field-effect gating of the materials, and there are no changes in doping level.

However, the situation is different when the physics are not known. Even if it is known that the relationships between the observables are linear, it is insufficient to establish the correct form of the functional dependence between them. In other words, any of the variables z_0, z_1, z_2 can be regressed on the remaining variables, as illustrated in Figs. 1(a)–1(c). For regression $z_0 = z_0(z_1, z_2)$, z_0 depends on z_1 according to the inverted Eq. (1a) and does not depend on z_2. However, while numerically correct, this relationship does not represent the physics of the process (i.e., the partial pressure of the gas does not depend on vacancy concentration). For regression $z_1 = z_1(z_0, z_2)$, the regression coefficients are close to zero and do not represent the physical relationship either. Only in the case of the regression $z_2 = z_2(z_0, z_1)$ are the regression coefficients meaningful and close to the ground truth Eqs. (1a) and (1b), as shown in

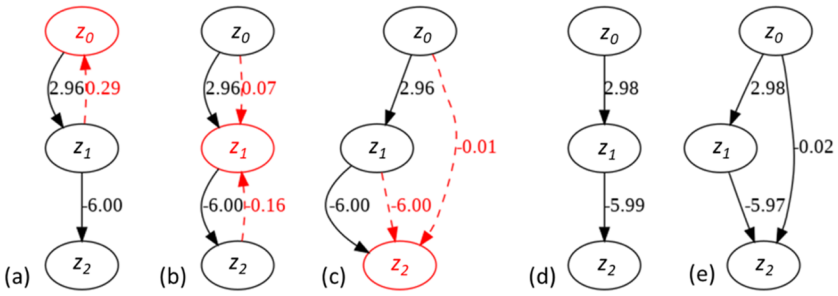

FIG. 1. Regression vs causal inference in a noisy toy model from a system of linear Eqs. (1a) and (1b). Shown are the causal chain and regression coefficients for regression of (a) $z_0(z_1, z_2)$, (b) $z_1(z_0, z_2)$, and (c) $z_2(z_0, z_1)$. In comparison, LiNGAM reconstruction using (d) a direct fit or (e) bootstrapping allows reconstruction of the causal chain from observational data (z_0, z_1, z_2).

Fig. 1(c). However, even in this case, based on the regression analysis only, we cannot answer questions such as "To what degree will the change of gas pressure affect the conductivity?" More fundamentally, from the data only, it is not clear which of the cases (a)–(c) should be chosen.

This behavior is well understood in statistics and illustrates the pitfalls of statistical analysis of data without a physical model, even for relatively trivial cases.[36,37] This situation can be much more complicated for a larger number of variables, in cases where the relationships between the variables are more complex, that is, the causal graph has a more complex structure, potentially including loops, non-linear relationships between variables, and external non-observed variables (confounders) that affect several of the observed variables. These considerations have stimulated the development of statistical methods for the analysis of causal structure in observational data, including the structure of the causal graph, the directionality of the causal effects, the presence of confounders, and the linear and non-linear relationships between the variables. A recent overview of these methods is given by Mooji *et al.*[38]

Here, we adopt the linear non-Gaussian acyclic model (LiNGAM) proposed by Shimizu for the analysis of time series data,[35,39–43] building upon the independent component analysis (ICA) by Oja.[44,45] LiNGAM specifically assumes that the relationships between the observed variables are linear, there are no external confounders, and the external influences are non-Gaussian, that is, the observations can be represented as

$$z = Az + \epsilon, \tag{2}$$

where **z** is the vector of observations, **A** is the adjacency matrix establishing the relationships between them, and $\boldsymbol{\epsilon}$ is the noise vector. Under the assumption of the directed causal graph, the matrix, **A**, has a lower diagonal shape. Correspondingly, LiNGAM seeks to find the linear decomposition of data via the ICA approach and then seeks to find the optimal representation of the link matrix via permutations.

For the toy model Eqs. 1(a) and 1(b), LiNGAM allows for the reconstruction of the causal graph between the variables. The reconstruction is shown in Figs. 1(d) and 1(e) for the bootstrapped and direct solution, respectively. Note that the algorithm established the causal graph and linear relationship coefficients between the variables based on observational data only.

We further explore the causal relationships in the $(Sm_xBi_{1-x})FeO_3$ (Sm-BFO) epitaxial thin-film system grown via a combinatorial spread method via LiNGAM, extending the previously reported pairwise causal analysis approach.[46] The growth details, preparation of the samples for STEM imaging, and initial data analysis and quantification are described in our previous

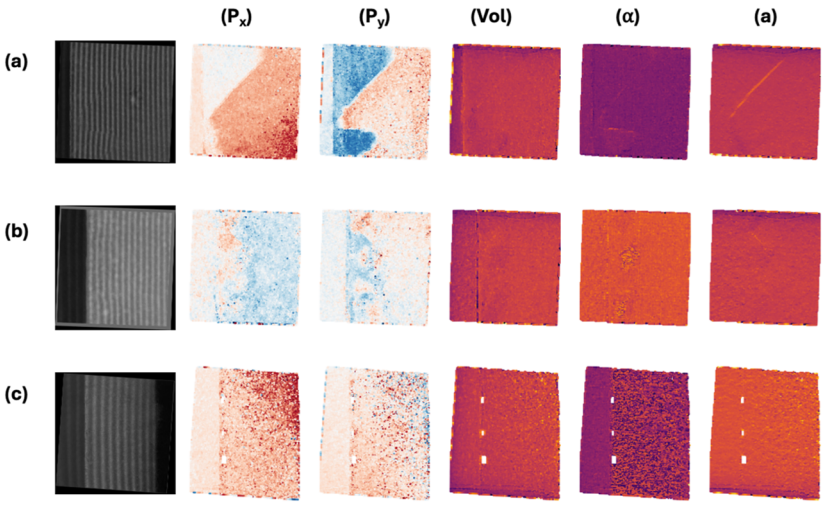

FIG. 2. STEM images and a partial set of order parameter maps for three Sm-BFO compositions explored: (a) $x = 0$, (b) $x = 0.07$, and (c) $x = 0.2$, corresponding to rhombohedral ferroelectric $BiFeO_3$, composition close to the morphotropic phase boundary, and orthorhombic antiferroelectric composition, respectively.

publications.[46–48] The full dataset is available as a part of the provided Jupyter notebook.

Here, we analyze the dependence of localized nominal physical properties such as polarization, lattice parameter, and chemical composition from the parameterization of atomic-scale HAADF-STEM images. For basic descriptors, we choose parameters from the 5-cation local neighborhood that are sensitive to cation composition: the total intensity of A-cation columns (Bi, Sm), I_{14}; intensity of B-site columns (Fe), I_5; to the structure: lattice parameters, a and b; unit-cell angle, α; and projected unit-cell volume, Vol; and to electrical polarization, components P_x and P_y, derived from non-centrosymmetry between the A and B sublattices. This vector (I_{14}, I_5, a, b, α, Vol, P_x, P_y) is defined for each unit cell within the field of view. The required conditions and preprocessing of the input STEM data used to ensure reliable parameterization are detailed in the supplementary material.

Shown in Fig. 2 are STEM images and a partial set of the order parameter maps for three compositions of the Sm-BFO chosen in Fig. 2(a), the ferroelectric region; Fig. 2(b), at the morphotropic phase boundary; and in Fig. 2(c), the orthorhombic phase. We note that the STEM images contain clearly visible spatial features, including ferroelectric and substrate regions and domain walls. In addition, more subtle variations in contrast due to second-phase inclusions, nanodomains, and surface preparation damage can be detected. Here, we aim to explore the causal relationship between the observables and further extend it for the analysis of spatially resolved features using the LiNGAM methods and codes developed by Shimizu.[49]

The LiNGAM method allows for the incorporation of prior knowledge in the form of defined causal relationships. Here, we postulate that the column intensities I_{14} and I_5 are independent variables, representing the combined effect of the sample

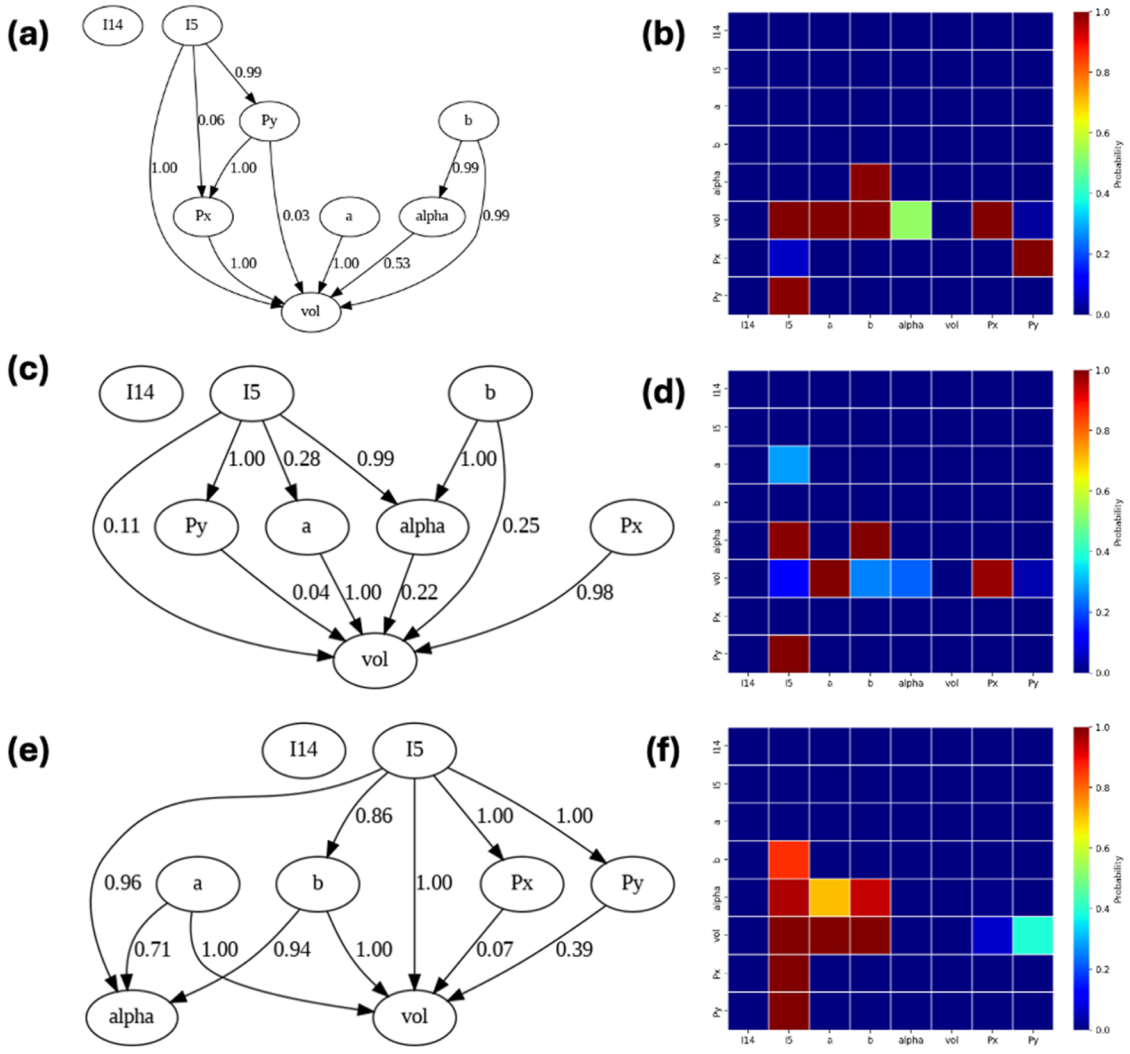

FIG. 3. Causal graphs and adjacency matrices for (a) and (b) ferroelectric, $x = 0$; (c) and (d) morphotropic, $x = 0.07$; and (e) and (f) orthorhombic, $x = 0.2$ compositions. Note: color encodes effect size ($|\beta i \to j|$) of each directed link (dark blue = 0, brighter = stronger).

thickness and the assumption of a frozen cation composition. With this approximation, the causal graph depicting the relationship between the variables for three representative compositions is shown in Fig. 3.

From the data shown in Fig. 3, the I_{14} variable does not causally affect any other variables. For the ferroelectric composition, $x = 0$, the control variables are P_y and b, which control P_x and α, respectively, which in turn control the projected unit-cell volume, *Vol*. The graphs for the non-ferroelectric compositions are almost identical, with the lattice parameters and polarization components being independent variables, and a and *Vol* being controlled. For the compositions at the morphotropic boundary and in the orthorhombic region, the causal graphs are almost identical, with the polarization and unit-cell parameters affected by the chemical variable and, in turn, controlling the unit-cell *Vol* and a. The corresponding linear regression coefficients in the form of adjacency matrices are shown in Figs. 3(b), 3(d), and 3(f). For comparison, all maps are shown at the same scale. Note the strong similarity between the elements, with the dominant coupling associated with the projected unit-cell volume, *Vol*.

We further extend this approach to explore the spatial variability in the thin films. To implement this approach, we extend the sliding window approach previously used in conjunction with Fourier or Radon transform/linear unmixing transformations.[25–27] Here, the image plane is subdivided into square tiles, and the LiNGAM analysis is performed within each tile. For convenience, we chose the stride of the tiles to be half of the tile size so that adjacent regions overlapped by 50%. Similar to the analysis of the whole image, the input is the (I_{14}, I_5, a, b, α, *Vol*, P_x, P_y) vector within the tile, and the outputs are the 8 × 8 adjacency matrices of the causal graph and the probability matrix.

The sliding analysis of the Sm-BFO composition is shown in Fig. 4. A simple examination of the images corresponding to the individual elements of the adjacency matrix illustrates that slightly over 50% are zero, corresponding to the absence of a local causal link between them. For several of the elements, including $Vol \leftarrow a$, $Vol \leftarrow b$, and $\alpha \leftarrow b$, the maps are almost uniform, without clearly visible structural elements. However, several of the maps exhibit visible structural features. For example, $Vol \leftarrow I_5$ and $P_y \leftarrow I_5$ maps clearly illustrate a feature at the interface between the film and the substrate. At the same time, $a \leftarrow b$ maps clearly illustrate a feature associated with the domain wall. Note that these links are bidirectional. We interpret this behavior as an indicator of a non-causal link between these parameters. The most remarkable contrast is observed in the $P_x \leftarrow P_y$ and $P_y \leftarrow P_x$ images, which illustrate the presence of a rich spatial structure. We attribute this behavior to the presence of disorder in the system that selectively affects the polarization components.

To gain further insight into the observed behaviors, we explore the spatial variability of the adjacency matrix using dimensionality reduction. Previously, these methods were extensively used for the analysis of hyperspectral imaging data in electron and

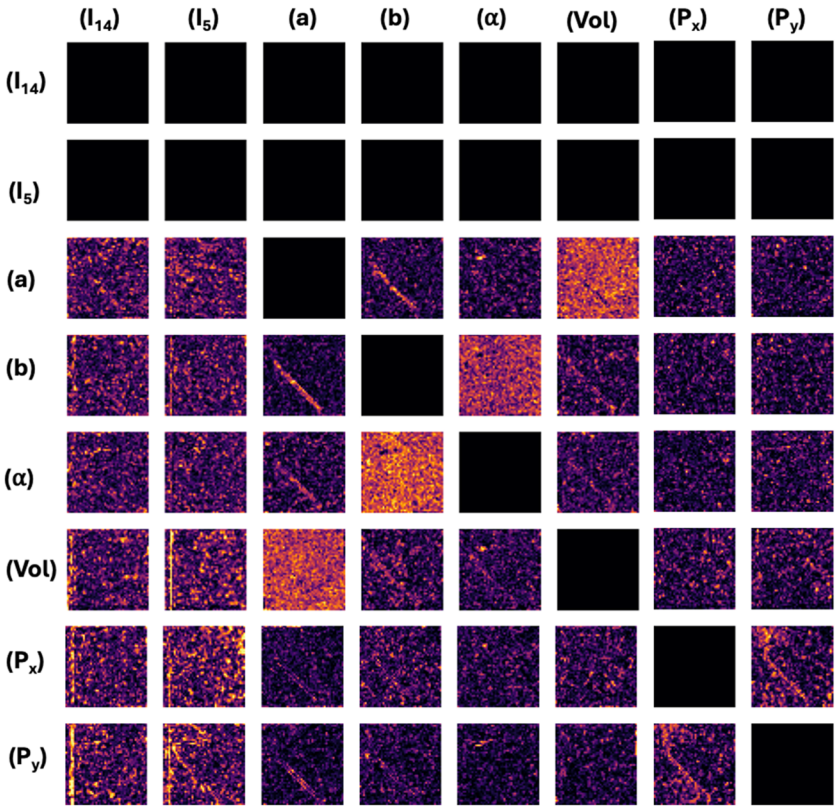

FIG. 4. Sliding window LiNGAM transforms on the $Sm_xBi_{1-x}FeO_3$ dataset for $x = 0$. Note that the use of a bootstrapping method for several variables leads to both $x \rightarrow y$ and $x \leftarrow y$ relationships: for example, for lattice parameters (a, b) and polarization components (P_x, P_y). We pose that this behavior indicates that variables are linked via a physical link but this link is non-causal (or cyclic).

scanning probe microscopies[50–55] and were later extended to sliding transform approaches. In principle, this can be implemented using linear methods such as principal component analysis (PCA), non-negative matrix factorization (NMF), or non-linear methods including Gaussian processing,[56,57] fully connected and variational autoencoders, or graph networks. Here, we choose PCA as the simplest method to perform optimal decomposition in the information theory sense—that is, with the components ranked in order of variability.

The PCA analysis for pure $BiFeO_3$ is shown in Fig. 5. Here, it is immediately obvious that the loading map corresponding to the first component exhibits variability at the interface between the film and the substrate, which is generally absent or much weaker in other loading maps. The corresponding component matrix is

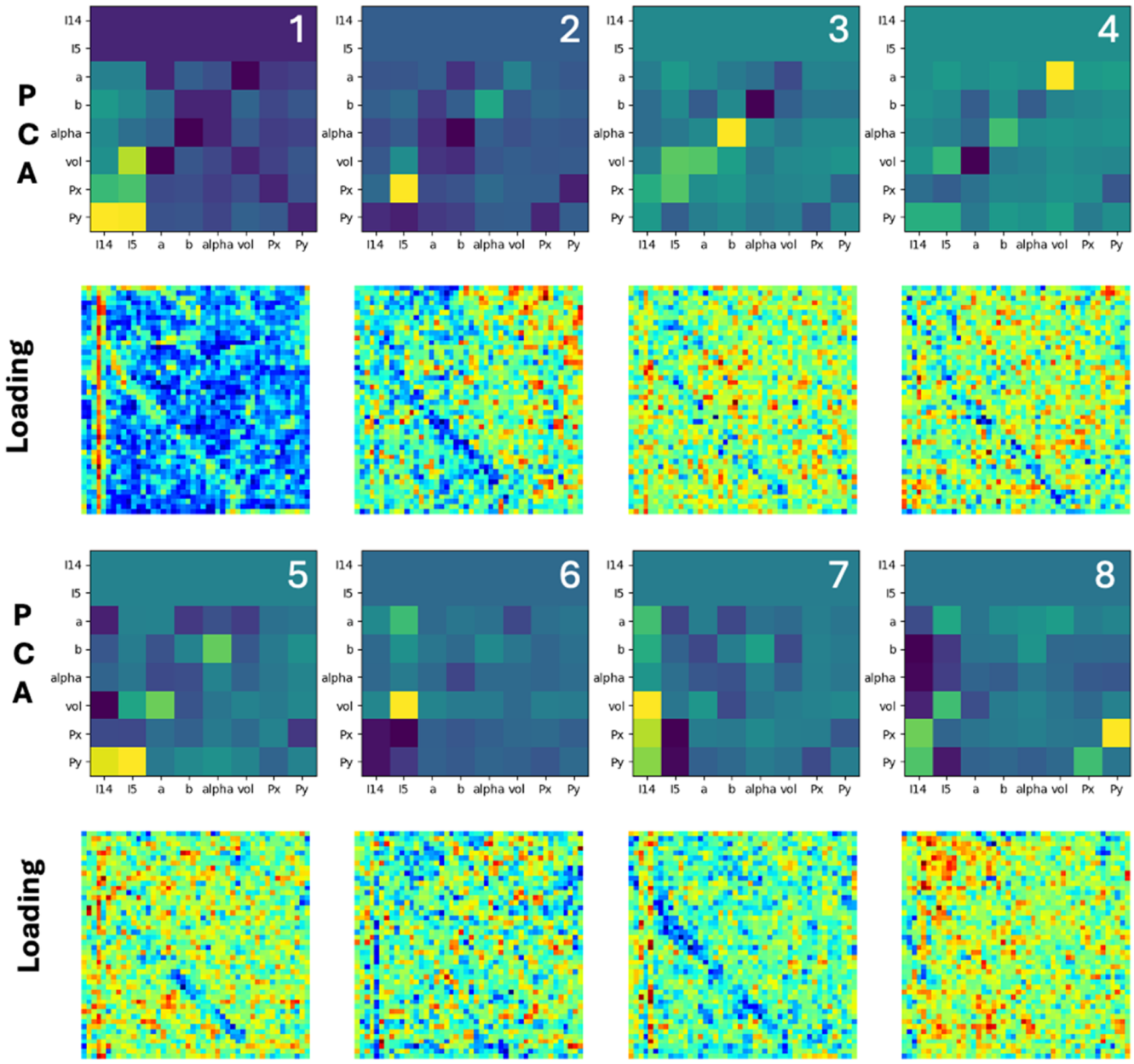

FIG. 5. PCA analysis of LiNGAM adjacency matrices for $BiFeO_3$. Shown are the first eight components and corresponding loading maps. The first component contains a clearly visible feature localized at the film–substrate interface, whereas the fourth, fifth, and seventh components clearly delineate the domain wall. Note: color encodes effect size ($|\beta i \to j|$) of each directed link (brighter = stronger).

dominated by coupling between I_5 and the polarization and projected volume, as well as between the volume and in-plane lattice parameter, a. The fourth, fifth, and seventh components exhibit visible features at the ferroelectric domain wall. The corresponding components are dominated by the couplings I_5–α, α–b, and I_{14}–I_5, respectively.

The sliding LiNGAM transform for the 20%-doped Sm-BFO (x = 0.2) is shown in Fig. 6. Similar to other compositions, here, the majority of the maps are either zero, indicating the absence of a causal link between the descriptors, or are spatially uniform. However, several of the elements exhibit non-trivial dynamics. Similar to other compositions, the $Vol \leftarrow I_5$ element visualizes a clearly visible feature at the domain wall. The $\alpha \leftarrow b$ map clearly visualizes the orthorhombic domains. Interestingly, the $\alpha \leftarrow P_x$ and $\alpha \leftarrow P_y$ maps illustrate spatial features associated with the wall between orthorhombic domains. Examination of the sliding transform for other explored compositions further reveals the presence of spatially ordered structures in some of the maps, suggesting the potential of this method to reveal internal structural relationships within the material.

Finally, we attempted to analyze the concentration dependence of the adjacency matrix, that is, the coupling strength between the observables. In this case, the analysis was performed over 13 independent STEM images corresponding to four different concentrations acquired over multiple days. In general, given the strong spatial variability within the dataset, we do not expect the statistics to be sufficient to discern the finer details of the concentration dependence; however, we expect the overall trends to be detectable. Examination of all 64 elements of the adjacency matrix demonstrated that most of these elements are either zero or constant. This suggests the universality of the corresponding couplings across the composition series. Non-trivial behaviors were observed for the $Vol \leftarrow a$, and $P_x \leftarrow P_y$ couplings, as shown in Fig. 7. For $Vol \leftarrow a$, we observe a minimum at the morphotropic phase boundary (MPB) composition. At the same time, $P_x \leftarrow P_y$ shows an effective change of sign from positive to negative at the MPB.

To explain these observations, we explore the relationships between the observable descriptors via the thermodynamic Landau–Ginzburg–Devonshire (LGD) theory. In LGD, the state of the system can be found via minimization of the free energy functional for defined global constraints. Here, we derive the local representation of LGD equations, linearize them around the ground states, and represent the relationship in the form of Eq. (1) with the observables in the STEM experiment being the state vector.

In the most general case, the description of rare-earth Sm-doped $BiFeO_3$ requires anti-ferrodistortive (AFD), ferroelectric (FE), and antiferroelectric (AFE) long-range order.[58–62] This necessitates two vectorial long-range order parameters: polarization components and oxygen octahedral tilts. The bulk part of the LGD thermodynamic potential consists of the following contributions:

$$G = \int d^3x (\Delta G_{AFD} + \Delta G_{BQC} + \Delta G_{FE} + \Delta G_{EST} + \Delta G_{EL}). \quad (3a)$$

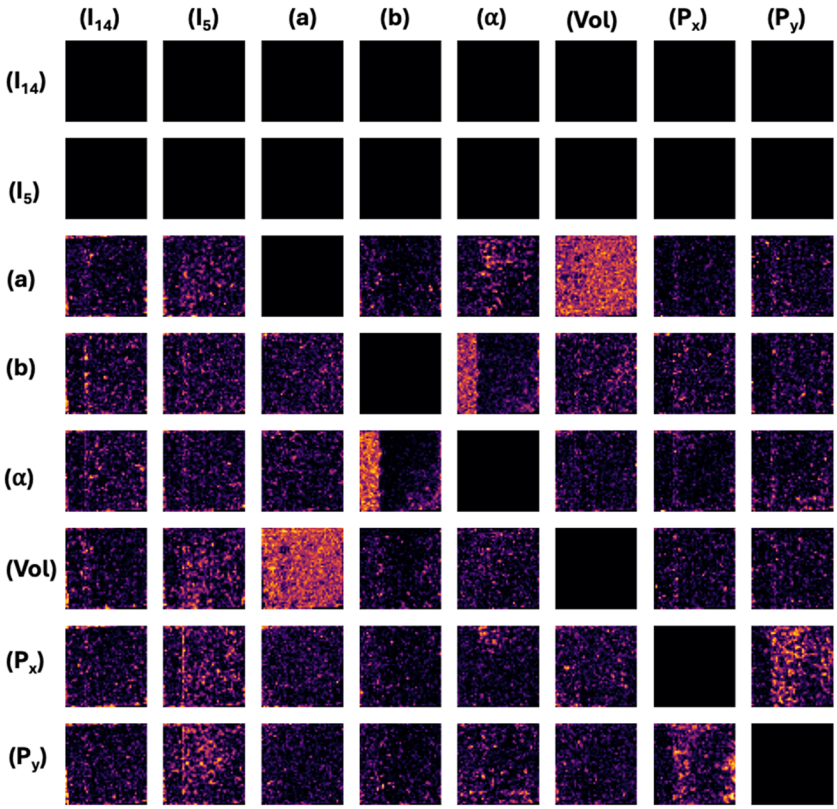

FIG. 6. Sliding window LiNGAM transform on the Sm-BFO dataset for x = 0.2 (orthorhombic phase).

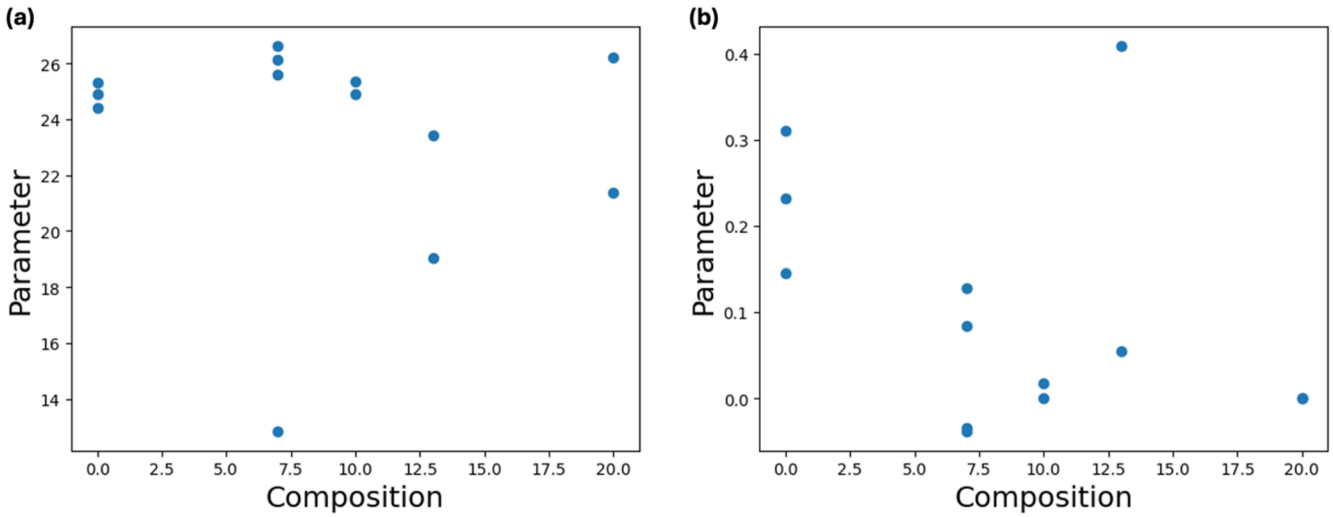

FIG. 7. Concentration dependence of (a) *Vol* ← *a* and (b) $P_x \leftarrow P_y$ couplings.

The compact form of the AFD contribution is given in Ref. 63. Operating at room temperature, we will assume that the main impact of the oxygen octahedral tilt is the renormalization of other coefficients in Eq. (1) due to the AFD–FE biquadratic coupling, ΔG_{BQC}. Since the oxygen octahedral tilts are hardly visible by the current realization of STEM, this circumstance allows us to factor out the non-observable variables from further consideration.

The compact forms of the FE and AFE contributions are

$$\begin{aligned}\Delta G_{FE} = {} & a_i\left(P_i^2 + A_i^2\right) + a_{ij}\left(P_i^2P_j^2 + A_i^2A_j^2\right) \\ & + a_{ijk}\left(P_i^2P_j^2P_k^2 + A_i^2A_j^2A_k^2\right) + \gamma_{ij}^{ab}\left(P_iP_j - A_iA_j\right) \\ & + g_{ijkl}^{aa}\left(\frac{\partial P_i}{\partial x_k}\frac{\partial P_j}{\partial x_l} + \frac{\partial A_i}{\partial x_k}\frac{\partial A_j}{\partial x_l}\right) \\ & + g_{ijkl}^{ab}\left(\frac{\partial P_i}{\partial x_k}\frac{\partial P_j}{\partial x_l} - \frac{\partial A_i}{\partial x_k}\frac{\partial A_j}{\partial x_l}\right),\end{aligned} \tag{3b}$$

where the FE and AFE order parameters, $P_i = \frac{1}{2}\left(P_i^a + P_i^b\right)$ and $A_i = \frac{1}{2}\left(P_i^a - P_i^b\right)$, respectively, are introduced. P_i^a and P_i^b are the polarization components of two equivalent sublattices, "*a*" and "*b*," respectively.[64] Numerical values of the phenomenological coefficients a_i, a_{ij}, a_{ijk}, and the gradient coefficients, g_{ij}, included in Eq. (3b) are mostly known for pure $BiFeO_3$ and can be found in supplementary material, Table SI.

The electrostriction contribution is

$$\Delta G_{EST} = -Q_{ijkl}^{aa}\sigma_{ij}\left(P_kP_l + A_kA_l\right) - Q_{ijkl}^{ab}\sigma_{ij}\left(P_kP_l - A_kA_l\right), \tag{3c}$$

where σ_{ij} are the components of the elastic stress tensor. Electrostriction coefficients are Q_{ijkl}^{aa} and Q_{ijkl}^{ab}. The elastic and flexoelectric contributions are

$$\Delta G_{EL} = -\frac{1}{2}s_{ijkl}\sigma_{ij}\sigma_{kl} - \frac{1}{2}F_{ijkl}\left(\sigma_{ij}\frac{\partial P_k}{\partial x_l} - P_k\frac{\partial \sigma_{ij}}{\partial x_l}\right) + V_{ij}\sigma_{ij}N_d. \tag{3d}$$

Here, s_{ijkl} are the components of the elastic compliance tensor, and F_{ijkl} are the flexoelectric tensor components. The last term in Eq. (3d) is the chemical expansion due to the appearance of elastic defects, that is, R-impurity with concentration, N_d, characterized by the Vegard strain tensor, V_{ij},[65,66] the value of which depends on the impurity and, as a rule, varies in the range $(-5\text{–}+5)\ 10^{-29}\ \mathrm{m}^3$. The full form of expressions (3) depends on the concrete form of the parent phase symmetry.

For a spatially uniform (i.e., domain-free) system, the equilibrium equations for the long-range order parameters can be found as partial derivatives of Eq. (3a), $\frac{\partial G}{\partial P_i} = 0$ and $\frac{\partial G}{\partial A_i} = 0$. These equations should be solved along with the equation of state for the elastic stress, $\frac{\partial G}{\partial \sigma_{ij}} = -u_{ij}$, where u_{ij} is an elastic strain tensor.

For the general case of an inhomogeneous (e.g., domain-structured and/or spatially modulated) system, one should solve the coupled Euler–Lagrange equations of state, which are expressed via the variational derivatives of the functional (3a):

$$\frac{\delta G}{\delta P_i} = -E_i, \quad \frac{\delta G}{\delta A_i} = 0. \tag{4a}$$

The electric field, E_i, can be found from electrostatic equations with boundary conditions at the surfaces, interfaces, and/or electrodes. Elastic fields, which are, in fact, the secondary order parameters, satisfy the equation of state and mechanical equilibrium equations:

$$\frac{\partial G}{\partial \sigma_{ij}} = -u_{ij}, \quad \frac{\partial \sigma_{ij}}{\partial x_j} = 0. \tag{4b}$$

The strains (or stresses) should be defined at the system boundaries. Coupled Eq. (4), which give us the relations between the primary and secondary order parameters, are listed in their explicit form in the supplementary material.

To link the standard thermodynamic descriptors to the observables, we use the relationships between the in-plane lattice constants, a, b, and the angle, α, between them:

$$a = a_0(1+u_{11}),\ \ b = b_0(1+u_{22}),\ \ cotan(\alpha) = u_{12}. \tag{5}$$

Here, a_0 and b_0 are the bulk values of undoped BFO at a given temperature. The projected volume of the 2D unit cell is $V = ab|\sin(\alpha)|$. The linearized changes of the unit-cell projected volume can be expressed via the 2D trace of the strain tensor:

$$V = ab|\sin(\alpha)| \approx a_0 b_0(1+u_{11}+u_{22}). \tag{6}$$

For high-resolution (HR)-STEM, the observable variables in Eqs. (5) and (6) are the in-plane components of the FE order parameters, P_1 and P_2, lattice constants, a, b, $\cos(\alpha)$, and changes of the projected unit cell volume, which, in principle, allow us to extract information about the joint action of the Vegard strain and electrostriction coupling. However, other components of the order parameters cannot be observed by HR-STEM imaging, which is why we need to find the simple (often approximate) linear relations between the observable and non-observable variables.

To do this, we linearized Eq. (4) in the vicinity of spontaneous values, denoted by subscript "S," which are

$$P_i = P_{Si}(\vec{x}) + \delta P_i, \quad A_i = A_{Si}(\vec{x}) + \delta A_i, \tag{7a}$$

$$u_{ij} = u^S_{ij}(\vec{x}) + \delta u_{ij}, \quad \sigma_{ij} = \sigma^S_{ij}(\vec{x}) + \delta\sigma_{ij}. \tag{7b}$$

The magnitudes of the spontaneous values, P_S or A_S depend on the average concentration of Sm dopant atoms, and the dependence can be modeled for the simplest linear model[67] as

$$P_S = P_0\sqrt{1-\epsilon}, \quad A_S = P_0\sqrt{1+\epsilon}, \tag{8}$$

where P_0 is the spontaneous polarization of bulk pure BFO (at a given temperature), and we introduced the dimensionless doping factor ϵ:

$$\epsilon(y) \cong \epsilon_0(y - y_0). \tag{9}$$

Here, y is the average Sm concentration in the studied sample, y_0 is a characteristic concentration corresponding to the MPB, and the FE and AFE phases have the same Curie temperatures. The coordinate dependence of the spontaneous values, $P_{Si}(\vec{x})$ and $A_{Si}(\vec{x})$, is related to mesoscale domain walls, while $\delta P_i(\vec{x})$ and $\delta A_i(\vec{x})$ are nanoscale fluctuations. Here, $\vec{x} = \{x_1, x_2\}$ is the in-plane coordinate vector.

Linearized Eqs. (3) and (4) can be written in the form of a 3 × 3 block-matrix containing nine equations:

$$\begin{pmatrix} a^P_{ij} - g^P_{ijkl}\dfrac{\partial^2}{\partial x_k \partial x_l} & 0 & 0 \\ 0 & a^A_{ij} - g^A_{ijkl}\dfrac{\partial^2}{\partial x_k \partial x_l} & 0 \\ q^P_{inj} + F_{injl}\dfrac{\partial}{\partial x_l} & q^A_{inj} & -1 \end{pmatrix} \begin{pmatrix} \delta P_j \\ \delta A_j \\ \delta u_{in} \end{pmatrix} = \begin{pmatrix} \delta E_i + Q^P_{mjki}P_{Sk}\delta\sigma_{mj} \\ Q^A_{mjki}A_{Sk}\delta\sigma_{mj} \\ V_{in}\delta N_d - s_{injm}\delta\sigma_{jm} \end{pmatrix}, \tag{10a}$$

where the block-matrix elements are

$$a^P_{ij} = 2\left(a_i + 3a_{il}P^2_{Sl} + 5a_{ilm}P^2_{Sl}P^2_{Sm}\right)\delta_{ij} + \left(\gamma^{ab}_{ij} - Q^P_{mlji}\sigma^S_{ml}\right), \tag{10b}$$

$$a^A_{ij} = 2\left(a_i + 3a_{ij}A^2_{Sj} + 5a_{ijk}A^2_{Sj}A^2_{Sk}\right)\delta_{ij} - \left(\gamma^{ab}_{ij} + Q^A_{mlji}\sigma^S_{ml}\right), \tag{10c}$$

$$q^P_{inj} = 2Q^P_{inkj}P_{Sk}, \quad q^A_{inj} = 2Q^A_{inkj}A_{Sk}. \tag{10d}$$

System (10) can be treated further analytically if we neglect the gradient terms, although the assumption is not well grounded everywhere. However, it can be valid if the coordinate dependence can be regarded as smooth and then ascribed to the domain wall profiles of $P_{Si}(\vec{x})$ and $A_{Si}(\vec{x})$, while the fluctuations, $\delta P_i(\vec{x})$ and $\delta A_i(\vec{x})$, are characterized by a short-range gradient with almost zero average. In this case, the antipolar order parameter can be expressed via other non-observable stress variations as $\delta A_n = \tilde{a}^A_{ni}Q^A_{mjki}A_{Sk}\delta\sigma_{mj}$, where $\tilde{a}^A_{mi}a^A_{ij} = \delta_{nj}$. Next, we exclude the non-observable variables from the left-hand side of Eq. (10a) by re-designation of the right-hand side:

$$e^*_i = \delta E_i + Q^P_{mjki}P_{Sk}\delta\sigma_{mj} - a^P_{i3}\delta P_3, \quad i = 1,2, \tag{11a}$$

$$s^*_{ij} = V_{in}\delta N_d + \left(s_{injm} + q^A_{imj}\tilde{a}^A_{ni'}Q^A_{mjki'}A_{Sk}\right)\delta\sigma_{jm} + q^P_{ij3}\delta P_3, \quad i,j = 1,2. \tag{11b}$$

The truncated matrix form is

$$\begin{pmatrix} a^P_{11} & a^P_{12} & 0 & 0 & 0 \\ a^P_{21} & a^P_{22} & 0 & 0 & 0 \\ -q^P_{111} & -q^P_{112} & 1 & 0 & 0 \\ -q^P_{121} & -q^P_{122} & 0 & 1 & 0 \\ -q^P_{221} & -q^P_{222} & 0 & 0 & 1 \end{pmatrix} \begin{pmatrix} \delta P_1 \\ \delta P_2 \\ \delta u_{11} \\ \delta u_{12} \\ \delta u_{22} \end{pmatrix} = \begin{pmatrix} e^*_1 \\ e^*_2 \\ s^*_{11} \\ s^*_{12} \\ s^*_{22} \end{pmatrix}. \tag{12}$$

Note that the in-plane strains in Eq. (12) are observable variables, namely, $\delta u_{11} = \frac{a}{a_0} - 1$, $\delta u_{12} = \cos(\alpha) \approx \frac{\pi}{2} - \alpha$, and $\delta u_{22} = \frac{b}{b_0} - 1$. Here, the projected volume, $V \approx ab$, since $\cos(\alpha) \approx \frac{\pi}{2} - \alpha$ is extremely small. Assuming zero spontaneous stresses and a m3m parent symmetry, the elements of the block matrix (12) are

$$a^P_{11} = a^P_{22} \approx 2a_1[1-\epsilon(y)] + 6a_{1l}P^2_{Sl}(\vec{x}) + \gamma^{ab}_{11}, \quad a^P_{12} = a^P_{21} = \gamma^{ab}_{12} = \gamma^{ab}_{21}, \tag{13a}$$

$$q^P_{111} = 2Q^P_{11}P_{S1}(\vec{x}), \quad q^P_{112} = 2Q^P_{12}P_{S2}(\vec{x}), \quad q^P_{121} = 2Q^P_{44}P_{S2}(\vec{x}), \tag{13b}$$

$$q^P_{122} = 2Q^P_{44}P_{S1}(\vec{x}), \quad q^P_{221} = 2Q^P_{12}P_{S1}(\vec{x}), \quad q^P_{222} = 2Q^P_{11}P_{S2}(\vec{x}). \tag{13c}$$

From this analysis, only the polarization dependence is expected to yield terms dependent on concentration, in agreement with observational studies.

We further proceed to explore possible mechanisms of spatial variability of observed behaviors. The coordinate dependence of the spontaneous values, $P_{Si}(\vec{x})$, related to a mesoscale domain wall in the direction x, perpendicular to the wall plane, $x = 0$, can be fitted by the following expression:

$$P_S(x) \cong \sqrt{-\frac{a_1}{a_{11}}}\sqrt{1-\epsilon(y)}\tanh\left(\frac{x}{L^P_C}\right). \tag{14}$$

Being repetitive, here, $\epsilon(y) \cong \epsilon_0(y - y_0)$, y is the average Sm concentration in the studied sample, y_0 is a characteristic concentration corresponding to the MPB, and the FE and AFE phases have the same Curie temperature. For a Sm-doped BFO, the value y_0 varies in the range of 15%–25% and the constant ϵ_0 must be fitted to experimental data. Parameters used in the LGD calculations for AFD-FE perovskite BFO are listed in Table SI; however, the AFE-FE coupling constants, γ_{ij}^{ab}, are unknown. The correlation lengths, L_C^P, in a rhombohedral ferroelectric are listed in Table SII in supplementary material.

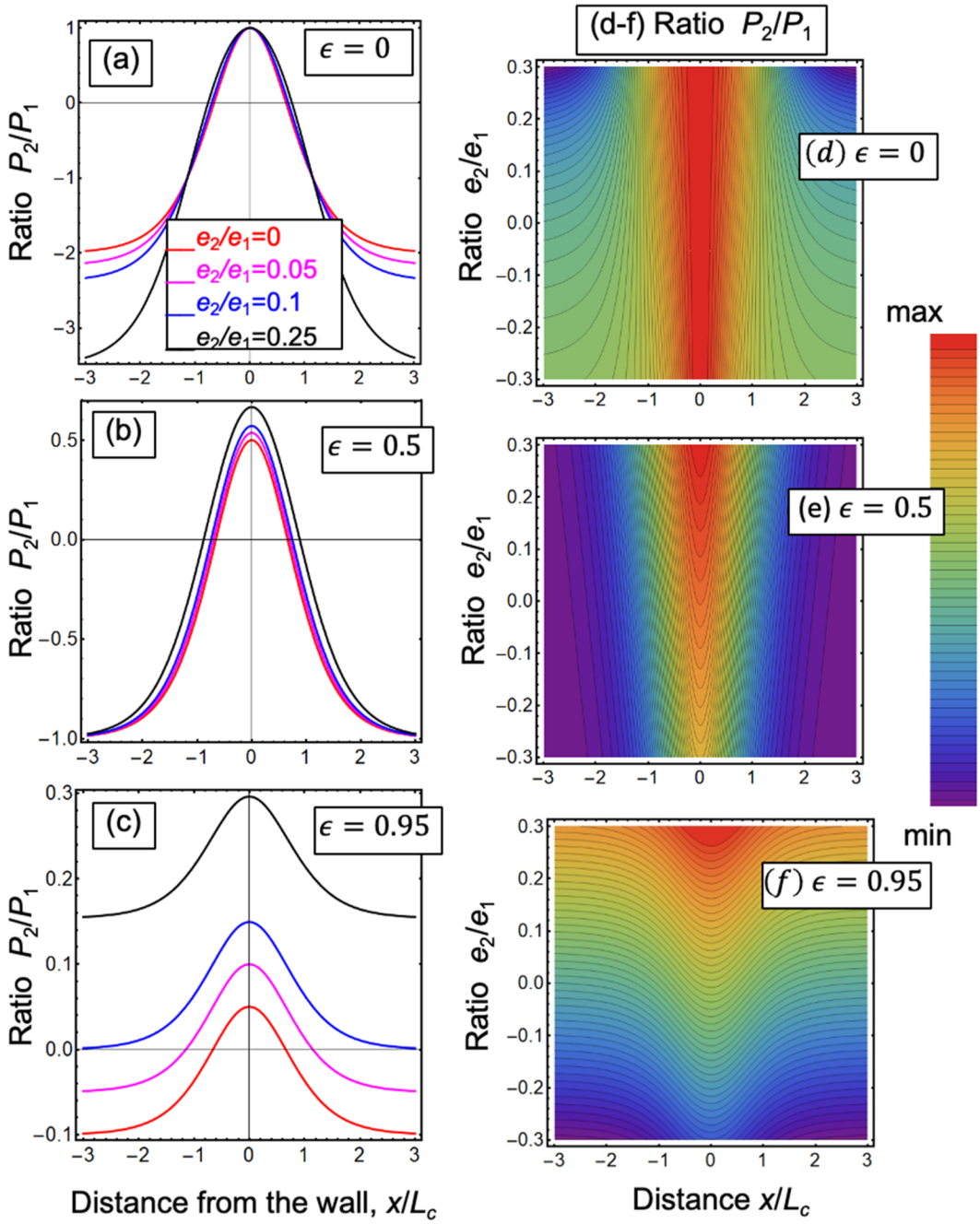

FIG. 8. Ratio of observable variables, $\delta P_2/\delta P_1$, dependence on distance, x/L_C^P, from the 180° domain wall calculated for different ratios of non-observable local fields, e_2^*/e_1^*, and different parameters, $\epsilon(y) = 0, 0.5, 0.95$, proportional to Sm concentration, y. (a)–(c) Linear plots. (d)–(f) Color maps. Red corresponds to maximal positive values; violet corresponds to minimal negative values. Other parameters, $a_{12}^P = a_{21}^P = -2a_1$.

For the sake of simplicity, we assume that $\delta\sigma_{mj} = 0$ and $\delta P_3 = 0$ when plotting Fig. 8. This immediately leads to $e_i^* = \delta E_i$, meaning that these non-observable variables are the components of local electric fields, and to $s_{ij}^* = V_{in}\delta N_d$, meaning that these non-observable variables are Vegard strains. If we also assume that $\gamma_{11}^{ab} = 0$, then $a_{11}^P = a_{22}^P = 2a_1[1-\epsilon(y)]\left(1 - 3tanh^2\left(\frac{x}{L_C^P}\right)\right)$ and thus, $a_{11}^P = a_{22}^P = -4a_1[1-\epsilon(y)] > 0$ far from the domain wall, while $a_{11}^P = a_{22}^P = 2a_1[1-\epsilon(y)] < 0$ at the wall.

Figure 8 illustrates how the dimensionless ratio, $\delta P_2/\delta P_1$, behaves under a change of the random field ratio, e_2^*/e_1^*, which is independent of the other observable variables, δu_{ij} (if the above assumptions are valid). From Eq. (12), we obtained the simple expressions:

$$\begin{aligned}\delta P_1 &= \frac{a_{11}^P e_1^* - a_{12}^P e_2^*}{\left(a_{11}^P\right)^2 - \left(a_{12}^P\right)^2},\\ \delta P_2 &= \frac{a_{11}^P e_2^* - a_{12}^P e_1^*}{\left(a_{11}^P\right)^2 - \left(a_{12}^P\right)^2},\\ \frac{\delta P_2}{\delta P_1} &= \frac{a_{11}^P\left(e_2^*/e_1^*\right) - a_{12}^P}{a_{11}^P - a_{12}^P\left(e_2^*/e_1^*\right)}.\end{aligned} \tag{15}$$

From Eq. (15) and Fig. 8, we observe that the dependence of $\delta P_2/\delta P_1$ on e_2^*/e_1^* reaches a maximum at the domain wall plane and the height of the maximum gradually decreases with an increase in $\epsilon(y)$. That said, the maximum at the wall is highest at the MPB, $\epsilon(y) = 0$. The sharpness of the maximum is virtually independent of $\epsilon(y)$. The ratio $\delta P_2/\delta P_1$ becomes much more sensitive to the ratio, e_2^*/e_1^*, as $\epsilon(y)$ increases. The limit, $\epsilon(y) \to 1$, corresponds to the AFE phase.

Note that the strains, δu_{ij}, are linearly dependent on the observable variables, δP_i, and seemingly independent of one another (while can be dependent via δP_i). Actually, from Eq. (12),

$$\begin{aligned}\delta u_{11} &= q_{111}^P \delta P_1 + q_{112}^P \delta P_2 + s_{11}^*,\\ \delta u_{12} &= q_{121}^P \delta P_1 + q_{122}^P \delta P_2 + s_{12}^*,\\ \delta u_{12} &= q_{121}^P \delta P_1 + q_{122}^P \delta P_2 + s_{12}^*.\end{aligned} \tag{16a}$$

For the case $P_{S1}(\vec{x}) = P_S(\vec{x})$ and $P_{S2}(\vec{x}) = 0$, corresponding to a single 180° domain wall in the x-direction, we obtain from Eq. (13) that $q_{111}^P = 2Q_{11}^P P_S(\vec{x})$, $q_{112}^P = 0$, $q_{121}^P = 0$, and $q_{122}^P = 2Q_{44}^P P_S(\vec{x})$, $q_{221}^P = 2Q_{12}^P P_S(\vec{x})$, $q_{222}^P = 0$, and so in the case of in-plane lattice parameters, the angle between them and the projected volume are the following:

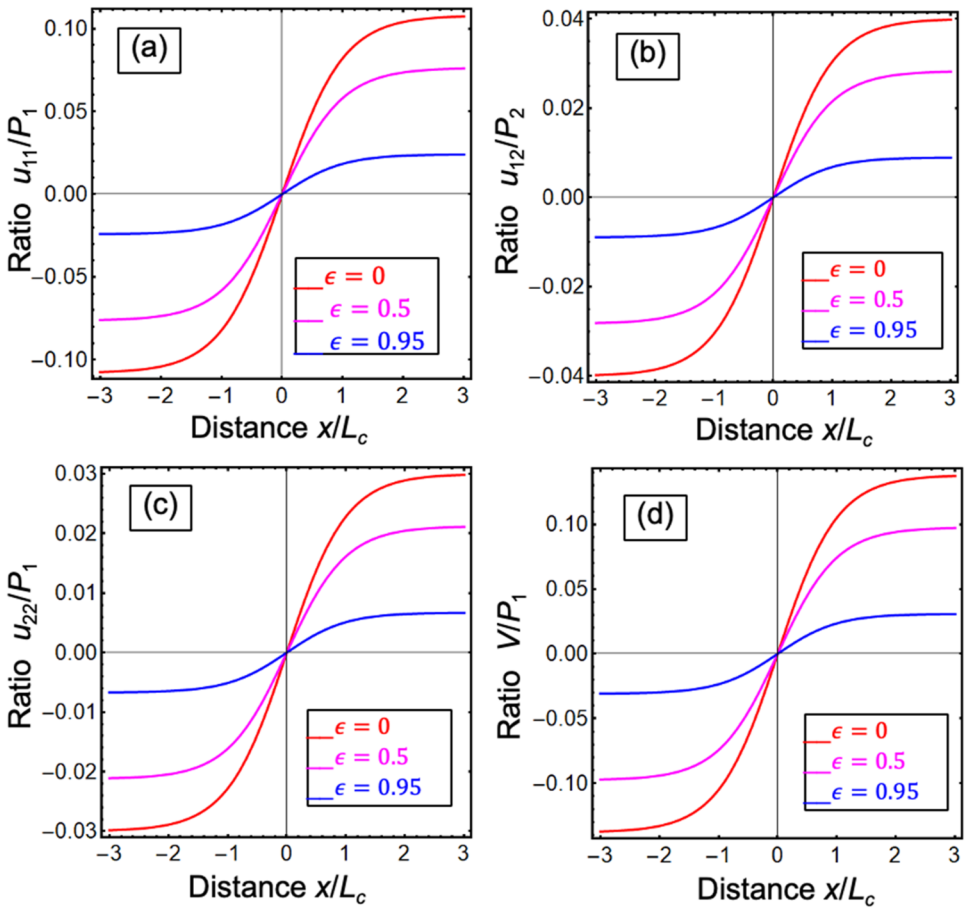

FIG. 9. Ratio of observable variables (a) $\delta u_{11}/\delta P_1$, (b) $\delta u_{12}/\delta P_2$, (c) $\delta u_{22}/\delta P_1$, and (d) $\delta V/\delta P_1$ in their dependence on distance, x/L_C^P, from the 180° domain wall calculated for different parameters, $\epsilon(y) = 0, 0.5, 0.95$, proportional to Sm concentration, y. Other parameters $a_{12}^P = a_{21}^P = -2a_1$, $s_{ij}^* = 0$.

$$\frac{a}{a_0} = 1 + 2Q_{11}^P P_S(\vec{x})\delta P_1 + s_{11}^*, \frac{b}{b_0} = 1 + 2Q_{12}^P P_S(\vec{x})\delta P_1 + s_{22}^*, \quad (16b)$$

$$\frac{\pi}{2} - \alpha = 2Q_{44}^P P_S(\vec{x})\delta P_2 + s_{12}^*,$$
$$\frac{V}{a_0 b_0} \approx 1 + 2\left(Q_{11}^P + Q_{12}^P\right)P_S(\vec{x})\delta P_1 + s_{11}^* + s_{22}^*. \quad (16c)$$

From the last expressions, $\frac{a}{a_0} - 1 \sim \delta P_1$ and $\frac{b}{b_0} - 1 \sim \delta P_1$, but $\frac{\pi}{2} - \alpha \sim \delta P_2$. Figure 9 illustrates the ratio of the observable variables, $\delta u_{11}/\delta P_1$, $\delta u_{12}/\delta P_2$, $\delta u_{22}/\delta P_1$, and $\delta V/\delta P_1$ in their dependence on the distance, x/L_C^P, from the 180° domain wall calculated for the different parameters, $\epsilon(y) = 0, 0.5, 0.95$, proportional to the Sm concentration, y. We put $a_{12}^P = a_{21}^P = -2a_1$ and $s_{ij}^* = 0$.

To summarize, here we explore the causal linear coupling between polarization, lattice parameter, and chemical composition from experimentally observed single unit-cell level behaviors in Sm-doped $BiFeO_3$. This analysis suggests that the causal links between the observables are nearly universal for all Sm concentrations/compositions. The variation of coupling strength between the different materials is generally similar across the phase transition boundary, with concentration-dependent behaviors observed for polarization only. This is directly confirmed by the linearized model based on the LGD theory for ferroelectrics. We further explored the spatial variability of the causal coupling using the sliding window transform method. Interestingly, this approach revealed new causal relationships emerging at both expected locations, such as domain walls and interfaces, but also at regions in the vicinity of the walls or spatially distributed features where clusters formed. While the exact physical origins of these relationships are unclear, they likely represent nanophase-separated regions in morphotropic phase boundaries.

Overall, we propose that an in-depth understanding of complex disordered materials necessitates the understanding of not only generative processes that can lead to observed microscopic states, but also the causal links between the observed variables. While generative models are sufficient to describe systems in the state of thermodynamic equilibrium, non-equilibrium systems may require causal descriptors that can describe cause-and-effect relationships between multiple interacting subsystems.

The supplementary material document for this publication provides additional details on the Ginzburg–Landau–Devonshire (LGD) thermodynamic model used to describe the physical system (S1), the derivation of the linearized equations relating observable and non-observable variables (S2–S3), and a comprehensive listing of the phenomenological parameters and correlation lengths used in the calculations (Tables SI–SII). It also includes a dedicated section (S4) outlining the specific data pre-requirements and optimal conditions for applying the LiNGAM model to experimental STEM data.

This effort was supported (S.V.K., I.T., and K.B.) as part of center for 3D Ferroelectric Microelectronics Manufacturing (3DFeM2), an Energy Frontier research Center funded by the U.S. Department of Energy (DOR), Ofiice of Science, Basic Energy Science under Award Number DE-SC0021118. STEM imaging (CN) was performed at the Oak Ridge National Laboratory's Center for Nanophase Materials Sciences (CNMS). A.N.M. and E.A.E. acknowledge funding from the DOE Software Project on "Computational Mesoscale Science and Open Software for Quantum Materials" (Award No. DE-SC0020145), under the Computational Materials Sciences Program of the U.S. Department of Energy, Office of Science, BES. The work at the University of Maryland was supported in part by the National Institute of Standards and Technology Cooperative Agreement No. 70NANB17H301 and the Center for Spintronic Materials in Advanced Information Technologies (SMART), one of the nCORE centers sponsored by the Semiconductor Research Corporation (SRC), the National Science Foundation (NSF), and NIST.

This manuscript has been authored by UT-Battelle, LLC, under Contract No. DE-AC0500OR22725 with the U.S. Department of Energy. The United States Government retains, and the publisher, by accepting the article for publication, acknowledges that the United States Government retains a non-exclusive, paid-up, irrevocable, worldwide license to publish or reproduce the published form of this manuscript, or allow others to do so, for the United States Government purposes. The Department of Energy will provide public access to these results of federally sponsored research in accordance with the DOE Public Access Plan (http://energy.gov/downloads/doe-public-access-plan).

AUTHOR DECLARATIONS

Conflict of Interest

The authors have no conflicts to disclose.

Author Contributions

Kamyar Barakati: Conceptualization (equal); Data curation (equal); Formal analysis (equal); Investigation (equal); Methodology (equal); Writing – original draft (equal). **Christopher T. Nelson**: Conceptualization (equal); Data curation (equal); Formal analysis (equal); Writing – original draft (equal). **Anna N. Morozovska**: Methodology (equal); Validation (equal); Visualization (equal). **Maxim A. Ziatdinov**: Conceptualization (equal); Formal analysis (equal); Investigation (equal); Methodology (equal). **Eugene A. Eliseev**: Formal analysis (equal); Investigation (equal); Methodology (equal). **Xiaohang Zhang**: Investigation (equal); Methodology (equal). **Ichiro Takeuchi**: Formal analysis (equal); Investigation (equal); Methodology (equal); Validation (equal). **Sergei V. Kalinin**: Conceptualization (equal); Formal analysis (equal); Funding acquisition (equal); Project administration (equal); Supervision (equal); Writing – review & editing (equal).

DATA AVAILABILITY

The data that support the findings of this study are available within the article and its supplementary material.

REFERENCES

[1] K. Binder and A. P. Young, Rev. Mod. Phys. **58**(4), 801–976 (1986).
[2] K. Binder and J. D. Reger, Adv. Phys. **41**(6), 547–627 (1992).
[3] A. Tagantsev, J. Fousek, and L. E. Cross, *Domains in Ferroic Crystals and Thin Films* (Springer, New York, 2010).

[4]B. E. Vugmeister and H. Rabitz, Phys. Rev. B **61**(21), 14448–14453 (2000).
[5]I. Grinberg, M. R. Suchomel, P. K. Davies, and A. M. Rappe, J. Appl. Phys. **98**(9), 094111 (2005).
[6]D. A. Keen and A. L. Goodwin, Nature **521**(7552), 303–309 (2015).
[7]A. K. Cheetham, T. D. Bennett, F. X. Coudert, and A. L. Goodwin, Dalton Trans. **45**(10), 4113–4126 (2016).
[8]A. R. Overy, A. B. Cairns, M. J. Cliffe, A. Simonov, M. G. Tucker, and A. L. Goodwin, Nat. Commun. **7**, 10445 (2016).
[9]C. Gerber and H. P. Lang, Nat. Nanotechnol. **1**(1), 3–5 (2006).
[10]G. Binnig, C. F. Quate, and C. Gerber, Phys. Rev. Lett. **56**(9), 930–933 (1986).
[11]G. Binnig, H. Rohrer, C. Gerber, and E. Weibel, Phys. Rev. Lett. **50**(2), 120–123 (1983).
[12]S. J. Pennycook and P. D. Nellist, *Scanning Transmission Electron Microscopy* (Springer, New York, 2011).
[13]O. L. Krivanek, M. F. Chisholm, V. Nicolosi, T. J. Pennycook, G. J. Corbin, N. Dellby, M. F. Murfitt, C. S. Own, Z. S. Szilagyi, M. P. Oxley, S. T. Pantelides, and S. J. Pennycook, Nature **464**(7288), 571–574 (2010).
[14]Y. Jiang, Z. Chen, Y. M. Hang, P. Deb, H. Gao, S. E. Xie, P. Purohit, M. W. Tate, J. Park, S. M. Gruner, V. Elser, and D. A. Muller, Nature **559**(7714), 343–349 (2018).
[15]M. J. Hytch and L. Potez, Philos. Mag. A **76**(6), 1119–1138 (1997).
[16]J. L. Taraci, M. J. Hytch, T. Clement, P. Peralta, M. R. McCartney, J. Drucker, and S. T. Picraux, Nanotechnology **16**(10), 2365–2371 (2005).
[17]M. J. Hytch, J. L. Putaux, and J. Thibault, Philos. Mag. **86**(29–31), 4641–4656 (2006).
[18]C. W. Zhao, Y. M. Xing, C. E. Zhou, and P. C. Bai, Acta Mater. **56**(11), 2570–2575 (2008).
[19]J. Kioseoglou, G. P. Dimitrakopulos, P. Komninou, T. Karakostas, and E. C. Aifantis, J. Phys. D: Appl. Phys. **41**(3), 8 (2008).
[20]V. Grillo and F. Rossi, Ultramicroscopy **125**, 112–129 (2013).
[21]Y. Zhu, C. Ophus, J. Ciston, and H. Wang, Acta Mater. **61**(15), 5646–5663 (2013).
[22]J. J. P. Peters, R. Beanland, M. Alexe, J. W. Cockburn, D. G. Revin, S. Y. Zhang, and A. M. Sanchez, Ultramicroscopy **157**, 91–97 (2015).
[23]A. A. Oni, X. Sang, S. V. Raju, S. Dumpala, S. Broderick, A. Kumar, S. Sinnott, S. Saxena, K. Rajan, and J. M. LeBeau, Appl. Phys. Lett. **106**(1), 4 (2015).
[24]D. Cooper, T. Denneulin, N. Bernier, A. Béché, and J.-L. Rouvière, Micron **80**, 145–165 (2016).
[25]R. K. Vasudevan, M. Ziatdinov, S. Jesse, and S. V. Kalinin, Nano Lett. **16**(9), 5574–5581 (2016).
[26]R. K. Vasudevan, A. Belianinov, A. G. Gianfrancesco, A. P. Baddorf, A. Tselev, S. V. Kalinin, and S. Jesse, Appl. Phys. Lett. **106**(9), 091601 (2015).
[27]N. Borodinov, W. Y. Tsai, V. V. Korolkov, N. Balke, S. V. Kalinin, and O. S. Ovchinnikova, Appl. Phys. Lett. **116**(4), 044103 (2020).
[28]B. R. Jany, A. Janas, and F. Krok, Micron **130**, 102800 (2020).
[29]W. Lin, Q. Li, A. Belianinov, B. C. Sales, A. Sefat, Z. Gai, A. P. Baddorf, M. Pan, S. Jesse, and S. V. Kalinin, Nanotechnology **24**(41), 415707 (2013).
[30]A. Belianinov, Q. He, M. Kravchenko, S. Jesse, A. Borisevich, and S. V. Kalinin, Nat. Commun. **6**, 7801 (2015).
[31]M. Ziatdinov, C. Nelson, R. K. Vasudevan, D. Y. Chen, and S. V. Kalinin, Appl. Phys. Lett. **115**(5), 052902 (2019).
[32]E. Dagotto, T. Hotta, and A. Moreo, Phys. Rep. **344**(1–3), 1–153 (2001).
[33]L. Vlcek, A. Maksov, M. Pan, R. K. Vasudevan, and S. V. Kalinin, ACS Nano **11**(10), 10313–10320 (2017).
[34]L. Vlcek, M. Ziatdinov, A. Maksov, A. Tselev, A. P. Baddorf, S. V. Kalinin, and R. K. Vasudevan, ACS Nano **13**(1), 718–727 (2019).
[35]S. Shimizu, P. O. Hoyer, A. Hyvarinen, and A. Kerminen, J. Mach. Learn. Res. **7**, 2003–2030 (2006).
[36]J. Pearl, J. Causal Inference **5**(2), 15 (2017).
[37]E. Bareinboim and J. Pearl, Proc. Natl. Acad. Sci. U. S. A. **113**(27), 7345–7352 (2016).
[38]J. M. Mooij, J. Peters, D. Janzing, J. Zscheischler, and B. Scholkopf, J. Mach. Learn. Res. **17**, 102 (2016).
[39]S. Shimizu, P. O. Hoyer, and A. Hyvarinen, Neurocomputing **72**(7–9), 2024–2027 (2009).
[40]A. Hyvarinen, K. Zhang, S. Shimizu, and P. O. Hoyer, J. Mach. Learn. Res. **11**, 1709–1731 (2010).
[41]S. Shimizu, T. Inazumi, Y. Sogawa, A. Hyvarinen, Y. Kawahara, T. Washio, P. O. Hoyer, and K. Bollen, J. Mach. Learn. Res. **12**, 1225–1248 (2011).
[42]S. Shimizu, Neurocomputing **81**, 104–107 (2012).
[43]S. Shimizu and K. Bollen, J. Mach. Learn. Res. **15**, 2629–2652 (2014).
[44]A. Hyvarinen and E. Oja, Neural Networks **13**(4–5), 411–430 (2000).
[45]A. Hyvarinen and E. Oja, Neural Comput. **9**(7), 1483–1492 (1997).
[46]M. Ziatdinov, C. T. Nelson, X. H. Zhang, R. K. Vasudevan, E. Eliseev, A. N. Morozovska, I. Takeuchi, and S. V. Kalinin, npj Comput. Mater. **6**(1), 9 (2020).
[47]C. T. Nelson, R. K. Vasudevan, X. H. Zhang, M. Ziatdinov, E. A. Eliseev, I. Takeuchi, A. N. Morozovska, and S. V. Kalinin, Nat. Commun. **11**(1), 12 (2020).
[48]M. Ziatdinov, N. Creange, X. Zhang, A. Morozovska, E. Eliseev, R. K. Vasudevan, I. Takeuchi, C. Nelson, and S. V. Kalinin, Appl. Phys. Rev. **8**(1), 011403 (2021).
[49]S. Shimizu, T. Inazumi, Y. Sogawa, A. Hyvarinen, Y. Kawahara, T. Washio, and P. Hoyer, "DirectLiNGAM: A direct method for learning a linear non-Gaussian structural equation model," J. Mach. Learn. Res. **12**, 1225–1248 (2011).
[50]N. Bonnet, J. Microsc. **190**, 2–18 (1998).
[51]N. Bonnet, in *Advances in Imaging and Electron Physics*, edited by P. W. Hawkes (Elsevier Academic Press Inc., San Diego, 2000), Vol. 14, pp. 1–77.
[52]S. Jesse and S. V. Kalinin, Nanotechnology **20**(8), 085714 (2009).
[53]R. Kannan, A. V. Ievlev, N. Laanait, M. A. Ziatdinov, R. K. Vasudevan, S. Jesse, and S. V. Kalinin, Adv. Struct. Chem. Imaging **4**, 20 (2018).
[54]M. Bosman, M. Watanabe, D. T. L. Alexander, and V. J. Keast, Ultramicroscopy **106**(11–12), 1024–1032 (2006).
[55]N. Dobigeon and N. Brun, Ultramicroscopy **120**, 25–34 (2012).
[56]Y. Altmann, N. Dobigeon, S. McLaughlin, and J. Y. Tourneret, IEEE Trans. Signal Process. **61**(10), 2442–2453 (2013).
[57]O. Eches, J. A. Benediktsson, N. Dobigeon, and J. Tourneret, IEEE Trans. Image Process. **22**(1), 5–16 (2013).
[58]I. O. Troyanchuk, D. V. Karpinsky, M. V. Bushinsky, O. S. Mantytskaya, N. V. Tereshko, and V. N. Shut, J. Am. Ceram. Soc. **94**(12), 4502–4506 (2011).
[59]A. Y. Borisevich, E. A. Eliseev, A. N. Morozovska, C. J. Cheng, J. Y. Lin, Y. H. Chu, D. Kan, I. Takeuchi, V. Nagarajan, and S. V. Kalinin, Nat. Commun. **3**, 775 (2012).
[60]E. A. Eliseev, S. V. Kalinin, Y. Gu, M. D. Glinchuk, V. Khist, A. Borisevich, V. Gopalan, L. Q. Chen, and A. N. Morozovska, Phys. Rev. B **88**(22), 224105 (2013).
[61]R. Maran, S. Yasui, E. A. Eliseev, M. D. Glinchuk, A. N. Morozovska, H. Funakubo, I. Takeuchi, and V. Nagarajan, Phys. Rev. B **90**(24), 11 (2014).
[62]R. Maran, S. Yasui, E. Eliseev, A. Morozovska, H. Funakubo, I. Takeuchi, and N. Valanoor, Adv. Electron. Mater. **2**(8), 1600170 (2016).
[63]E. A. Eliseev, A. N. Morozovska, C. T. Nelson, and S. V. Kalinin, Phys. Rev. B **99**(1), 17 (2019).
[64]C. Kittel, Phys. Rev. **82**(5), 729–732 (1951).
[65]D. A. Freedman, D. Roundy, and T. A. Arias, Phys. Rev. B **80**(6), 064108 (2009).
[66]Y. Kim, A. S. Disa, T. E. Babakol, and J. D. Brock, Appl. Phys. Lett. **96**(25), 251901 (2010).
[67]A. N. Morozovska, E. A. Eliseev, D. Y. Chen, V. Shvetz, C. T. Nelson, and S. V. Kalinin, Phys. Rev. B **102**(7), 14 (2020).